

1

2 **Modeling transpiration with sun-induced chlorophyll fluorescence via water use** 3 **efficiency and stomatal conductance**

4 **Huaize Feng¹, Tongren Xu¹, Xinlei He¹, Jingxue Zhao¹, Shaomin Liu¹**

5 ¹ State Key Laboratory of Earth Surface Processes and Resource Ecology, School of Natural
6 Resources, Faculty of Geographical Science, Beijing Normal University, Beijing 100875, China

7 **Key Points:**

8 • Transpiration can be modeled accurately by SIF observations via water use efficiency and
9 stomatal conductance methods.

10 • Mechanism models outperformed the linear models for monitoring transpiration.

11 • Air dryness has an important impact on the relationship between transpiration and SIF.

12 **Abstract**

13 Successfully applied in the carbon research area, sun-induced chlorophyll fluorescence (SIF) has
14 raised the interest of researchers from the water research domain. However, the mechanism
15 between SIF emitted by plants and transpiration (T) has not been fully explored. To improve the
16 understanding of the relationship between SIF and T, we developed two SIF-T models, namely the
17 WUE model and conductance model, based on carbon-water coupling framework. Hourly data
18 observation at 4 sites were used to develop and validate the model, which were covered C3 and
19 C4 plants. Compared with traditional model, results show that the developed WUE model and
20 conductance model have higher R^2 and lower RMSE. The developed models further indicate the
21 potential and mechanism in estimating water flux by remotely sensed SIF observations.

22 **1 Introduction**

23 Evapotranspiration (ET) is not only a pipeline of the water cycle in the air but also an important
24 influence factor of energy balance as a carrier of latent heat. Previous works indicated transpiration
25 (T) occupies a dominant position in evapotranspiration [*Good et al.*, 2015; *Jasechko et al.*, 2013].

26 In some ecosystems, T could reach 95% of the total ET [Stoy *et al.*, 2019]. T is also closely coupled
27 with the carbon plant productivity [Kool *et al.*, 2014]. Therefore, an accurate understanding of the
28 spatiotemporal changes of T is crucial for understanding the substance and energy interactions
29 between the land surface and the atmosphere.

30 In this century, Sun-induced chlorophyll fluorescence (SIF) renewed the gross primary
31 production (GPP) estimation from ground to space [Frankenberg and Berry, 2018; Ryu *et al.*, 2019;
32 Schimel *et al.*, 2019]. Considering the connection between photosynthesis and transpiration, SIF
33 may serve as a pertinent constrain estimates for transpiration. [Alemohammad *et al.*, 2017; Jonard
34 *et al.*, 2020]. Recently, Empirical analysis based on ground and remote sensing SIF observation
35 showed SIF is strongly related to T, [Lu *et al.*, 2018] reconstructed the full band SIF and exploit
36 the capacity of individual SIF bands and their combinations for deriving T with empirical linear
37 regression and Gaussian Process Regression model at Harvard Forest. [Pagán *et al.*, 2019] used
38 radiation corrected GOME-2 SIF observations to diagnose transpiration efficiency understood as
39 the ratio between transpiration and potential evaporation worldwide. [Maes *et al.*, 2020]
40 investigated the empirical link between SIF and T using satellite SIF (GOME-2 and OCO-2) and
41 SCOPE model at sites from FLUXNET. However, the studies mentioned above relate T with SIF
42 empirically, not mechanistically. SIF is the light signal from the excited chlorophyll a molecules
43 after absorption of photosynthetically active radiation. The information about the electron
44 transport (J) from photosystem II to photosystem I contained in SIF makes the signal a powerful
45 tool to predict GPP [Gu *et al.*, 2019; Köhler *et al.*, 2018; Zhang *et al.*, 2014]. Furthermore, the
46 essential of understanding the SIF-T relationship should lie in the coupling between the carbon
47 and water cycles.

48 The carbon and water cycles between the biosphere and atmosphere are strongly coupled
49 [*Gentine et al.*, 2019]. The trade-off between photosynthesis and water vapor loss is arguably the
50 most central constraint on plant function [*Wolz et al.*, 2017]. Water-use efficiency (WUE) and
51 stomatal conductance (g_s , or canopy conductance, g_c) are two key metrics of carbon - water
52 coupling. WUE is defined as the amount of carbon assimilated relative to water use [*Leakey et al.*,
53 2019]. [*Maes et al.*, 2020] reported WUE and related variables show a most important impact on
54 the SIF-T relation. Plants take in carbon dioxide and breath out water through stomata
55 simultaneously. Stomata played a key role in the carbon-water coupling, even the whole Earth
56 System [*Berry et al.*, 2010]. By analyzing the empirical link of SIF and canopy conductance, [*Shan*
57 *et al.*, 2019] reported the empirically linear linkage between g_s and SIF data from C3 forest,
58 cropland, and grassland ecosystems, and T calculated by SIF-based conductance agreed well with
59 ET observed by flux towers.

60 Even though some studies have been conducted for T estimation based on SIF observations,
61 they usually use the empirical method. It is unclear how can WUE and g_s be used to model T by
62 SIF mechanistically. In this paper, two carbon-water coupling indicators: water use efficient and
63 stomatal conductance are introduced to clarify the physical relevance between SIF and T. Using
64 the concept of these two indicators, two mechanism SIF-T models are built and tested based on
65 hourly ground observations at four sites, including two C4 and two C3 sites. The results are
66 expected to improve our understanding of the link between SIF and T.

67 **2 Materials and Methods**

68 2.1 Materials

69 SIF and corresponding observation (eg. meteorological variables, flux observation, and
70 vegetation indexes) are acquired at four sites including two maize field sites (Daman from Heihe

71 river basin, China, DM; Huailai from Haihe river basin, China, HL), one temperate deciduous
72 forest site (Harvard Forest from AmeriFlux network, US, HF), and a subalpine conifer forest
73 (Niwot Ridge from AmeriFlux network, US, NR). The characteristics of these sites are
74 summarized in Table 1. The SIF measurements of DM and HL sites (760 nm) were conducted
75 using a tower-based automatic measurement system named “SIFSpec” [Du *et al.*, 2018] and
76 retrieved using the 3FLD method [Liu *et al.*, 2020]. The SIF data (745- to 758-nm) of NR were
77 from a scanning spectrometer (PhotoSpec) on the top of the 26 meters tower. SIF data in winter
78 were abandoned in this study because the subalpine trees at the NR site undergone significant
79 physiological stress during the cold climate [Magney *et al.*, 2019]. The SIF data of HF were
80 retrieved from FluoSpec deployed about 5 m above the canopy on the top of a tower and extracted
81 by spectral fitting methods at 760 nm [Yang *et al.*, 2015].

82 Meteorological variables include net radiation (Rn), relative humidity and so on (See Table
83 2). Latent heat (LE) and net ecosystem exchange (NEE) are taken from flux observed by Eddy
84 Covariance towers. Gross primary production (GPP) was separated from net ecosystem exchange
85 (NEE) following [Reichstein *et al.*, 2005] and [Lasslop *et al.*, 2010] via the REddyProcWeb online
86 tool (https://www.bgcjena.mpg.de/bgi/index.php/Services_/REddyProcWeb). Leaf area index
87 (LAI) of all four sites was acquired from the MCD15A3H dataset with 4-day and 500 m temporal-
88 spatial resolution [Myneni *et al.*, 2015] and interpolated to hourly scale on Google Earth Engine
89 [Gorelick *et al.*, 2017]. One hour before the rainfall and six hours after the rainfall data were
90 excluded to minimize the influence of canopy interception.

91 T modeled by SIF is evaluated by T_{Zhou} partitioned from ET. [Zhou *et al.*, 2014] proposed an
92 index called underlying water-use efficiency (uWUE) by combining the optimal stomatal behavior
93 model with Fick's law. This method was developed based on flux tower data of 14 sites, including

94 the HF site, and successfully applied to Heihe River Basin [Zhou *et al.*, 2018], including the DM
 95 site. Especially, at the DM site, T/ET estimated by the uWUE method agreed with the isotope
 96 method well during the peak growing season [Bai *et al.*, 2019].

97 2.2 WUE Model

98 SIF and GPP can both be represented in the form of light use efficiency (LUE) model:

$$99 \text{SIF} = \text{APAR} \Phi_F \Omega_c \quad (1)$$

$$100 \text{GPP} = \text{APAR} \text{LUE} \quad (2)$$

101 where APAR stands the photosynthetically active radiation absorbed by photosynthetic
 102 pigments, Φ_F is the fluorescence quantum yield, and Ω_c is the probability of SIF photon escaping
 103 from the canopy. Combining Eqn 1 with Eqn 2, we can obtain a linear model between SIF and
 104 GPP:

$$105 \text{GPP} = \text{SIF} \frac{\text{LUE}}{\Phi_F \Omega_c} \quad (3)$$

106 where LUE is the light-use-efficiency. Based on previous works [Guanter *et al.*, 2014; Li *et al.*,
 107 2018; Sun *et al.*, 2017; Liu *et al.*, 2017; Magney *et al.*, 2019; Yang *et al.*, 2015], the factor $\frac{\text{LUE}}{\Phi_F \times \Omega_c}$
 108 can be set as a constant for a specific plant type, and GPP can be calculated by SIF directly. For
 109 C3 and C4 plants, WUE is relatively stable. Many works derived T from GPP by treating WUE as
 110 a constant value during certain period [Scott and Biederman, 2017; Yang *et al.*, 2015]. Under this
 111 assumption T can be calculated by SIF via the following equation:

$$112 \text{GPP}_{\text{linear}} = k1 \text{SIF} \quad (4)$$

$$113 \text{T}_{\text{linear}} = k2 \text{GPP}_{\text{linear}} \quad (5)$$

114 where k1, k2 are two parameters denoting $\frac{\text{LUE}}{\Phi_F \times \Omega_c}$ and WUE respectively. Eqn 5 is the theory base
 115 of the empirical linear relationship between SIF and T.

116 However, WUE is strongly affected by the dryness of air from leaf to ecosystem scale. The
 117 relationship between GPP and T improved significantly by incorporating the effects of the vapor
 118 pressure deficit (VPD) from diurnal to annual time scales [Beer et al., 2009; Zhou et al., 2014].
 119 Moreover, [Jonard et al., 2020] pointed out the atmospheric demand for water helps explaining a
 120 lot variability in the SIF–T relationship at the ecosystem scale. Here we proposed a WUE model:

$$121 \quad \text{GPP}_{\text{WUE}} = k3 \text{ SIF} \quad (6)$$

$$122 \quad \text{T}_{\text{WUE}} = k4 \text{ VPD}^{k5} \text{ GPP}_{\text{WUE}} \quad (7)$$

123 where k3 is a parameter like k1. k4 is a parameter concluding information on water-use efficiency.
 124 k5 quantifies of the non-linear effect of VPD on k4 [Lin et al., 2018]. In this work, VPD is
 125 calculated from air temperature and relative humidity of air.

126 2.3 Conductance Model

127 Though the linear SIF-GPP relationship (Eqn 3) looks simple, the mechanism of the
 128 parameter LUE in is complex. Φ_f and Ω_c are relatively stable value [Guanter et al., 2014; Tol et
 129 al., 2014], and LUE is often calculated by reducing potential LUE using several environmental
 130 factors, such as temperature, soil moisture [Yuan et al., 2007]. Previous work had also reported the
 131 hyperbolic relationship between SIF and GPP [Damm et al., 2015; Zhang et al., 2020]. Therefore,
 132 the relationship between SIF and GPP is far more complicated than linear. The link between SIF
 133 and GPP is because of the close relationship between SIF and electron transport rate (J) and J can
 134 be derived by SIF in [Gu et al., 2019]:

$$135 \quad J = a q_L \text{ SIF} \quad (8)$$

136 Benefit from the carbon-pump mechanism, the GPP of C4 plants is linearly related to. For C4
 137 plants[Collatz et al., 1992], GPP can be derived by:

$$138 \quad \text{GPP}_{\text{gs}} = J/4 = \frac{a q_L \text{ SIF}}{4\Omega_c} \quad (9)$$

139 a is an empirical factor supposed to be a constant under ideal environments, q_L is the fraction of
 140 open Photosynthesis II reaction centers, indicating the 'traffic jam' in the electron transport
 141 pathway from Photosystem II to Photosystem I. Note that, the Eqn 8 is designed for broadband
 142 SIF for PSII. In this paper, single NIR band SIF is used instead by assuming a linear relationship
 143 between single-band SIF and full band SIF. q_L ranges from 0-1 and decreases with increased PAR
 144 [Baker, 2008; Gu et al., 2019]. In this paper, q_L is derived by:

$$145 \quad q_L = \exp(-\beta \text{PAR}) \quad (10)$$

146 β is a parameter denoting the sensitivity of q_L to the illumination. Due to data restrictions, Ω_c for
 147 the near-infrared band SIF was set as a constant in our study. g_s for C4 plants is derived by inserting
 148 Eqn into the famous Ball-Berry model [Ball et al., 1987]:

$$149 \quad g_s = m \frac{a q_L \text{SIF}}{4\Omega_c} \text{Rh}/C_a + g_0 \quad (11)$$

150 where m is an empirical slope parameter, which is often treated as a constant for a specific
 151 ecosystem [Miner et al., 2017]. C_a is the ambient carbon dioxide concentration and g_0 is the
 152 minimum conductance which is set as 0. Lack of an efficient mechanism gathering CO_2 from the
 153 air, C3 plants much more rely on the stomata to absorb CO_2 for the Calvin cycle. For C3 plants,
 154 the relationship between SIF and GPP is also affected by the dark reactions. The relationship
 155 between GPP and SIF for C3 can be expressed by [Gu et al., 2019]:

$$156 \quad \text{GPP}_{g_s} = a \frac{C_i - \Gamma^*}{4C_i + 8\Gamma^*} q_L \text{SIF} \frac{1}{\Omega_c} \quad (12)$$

157 C_i is the intercellular CO_2 concentration. Γ^* is the CO_2 compensation point in the absence of
 158 mitochondrial respiration, which can be set as a constant for specific plant type or calculated by
 159 air temperature [Katul et al., 2010]. C_i can be eliminated by combining Eqn 12 with Fick's law
 160 $\text{GPP} = g_s \times (C_i - C_a)$, then we have:

$$161 \quad GPP_{gs} = a \frac{GPP/g_s + C_a - \Gamma^*}{4(GPP/g_s + C_a) + 8\Gamma^*} q_L SIF \frac{1}{\Omega_c} \quad (13)$$

162 g_s and GPP_{gs} can be solved under the constraining of the optimality theory of stomatal behavior.

163 [*Cowan and GD, 1977; Katul et al., 2010; Way et al., 2014*]. According to this theory, plants tend

164 to adapt stomata to minimize the cost of water while maximizing carbon assimilation:

$$165 \quad f(g_s) = GPP - \lambda ET \approx GPP - 1.6\lambda g_s VPD/P \quad (14)$$

$$166 \quad \delta f(g_s)/\delta(g_s) = 0 \quad (15)$$

167 λ represents the marginal water cost of carbon assimilation. P is the air pressure. If we incorporate

168 [Eqn 13, 14, and 15](#), g_s can be expressed as the function \mathcal{F} of SIF, q_L , λ , Γ , VPD and C_a :

$$169 \quad g_s = \mathcal{F}(SIF, q_L, \lambda, \Gamma, VPD, C_a)$$

$$170 \quad = -\frac{a SIF q_L (4\Gamma - C_a)}{4(2\Gamma + C_a)^2} + \frac{a SIF q_L (2\Gamma + C_a - 3.2\lambda VPD) \sqrt{3.2\lambda VPD \Gamma (C_a - \Gamma) (2\Gamma + C_a - 1.6VPD\lambda)}}{6.4\lambda VPD (2\Gamma + C_a)^2 (2\Gamma + C_a - 1.6\lambda VPD)} \quad (16)$$

171 Finally, with SIF-based g_s , T can be calculated by the two-source Penman-Monteith method

172 [*Leuning et al., 2008*]:

$$173 \quad Ac = R_n \times [1 - \exp(-0.5LAI) / \cos(SZA)] \quad (17)$$

$$174 \quad T_{gs} = \frac{\Delta Ac + \rho C_p VPD g_a}{\Delta + \gamma \left(1 + \frac{g_a}{g_s}\right)} \quad (18)$$

175 [Eqn 17](#) is the simple one-dimensional Beer's law model. Ac is the available energy of the canopy

176 layer, R_n is net radiation, LAI is the leaf area index and SZA is the sun zenith angle. For [Eqn 18](#),

177 Δ is the rate of change of vapor pressure with temperature, γ is the psychrometric constant, C_p is

178 the specific heat of air; ρ is the density of liquid water, and g_a is aerodynamic conductance.

179 2.3 Model Calibration

180 Parameters of both the WUE model and the conductance model need to be calibrated (see

181 [Table 3](#)). GPP and the water balance framework are used here to constrain the models. Total ET

182 observed by eddy covariance measurement is composed of plant transpiration (T) and soil
183 evaporation (LEs):

$$184 \quad \quad \quad LE = T + LEs \quad \quad \quad (19)$$

185 LEs can be calculated by soil available energy (see Table 2). Considering the nonlinearity and
186 complicity of the models, the shuffled complex evolution (SUE-UA) algorithm [Duan *et al.*, 1994]
187 is employed to fit parameters by maximizing the cost function G:

$$188 \quad \quad \quad G = 0.4NSE(GPP_{ob}, GPP_{model}) + 0.6NSE(LE_{ob}, LE_{model}) \quad \quad \quad (20)$$

189 where NSE is the Nash-Sutcliffe efficiency coefficient. The subscript _{ob} means observed values
190 and variables with a subscript _{model} mean values are derived by models described above. All model
191 estimations and statistical analyses were performed with Python 3.8.3 [Harris *et al.*, 2020; Herman
192 and Usher, 2017; Houska *et al.*, 2015]. The description and calculation of all variables mentioned
193 above are listed in Table 2.

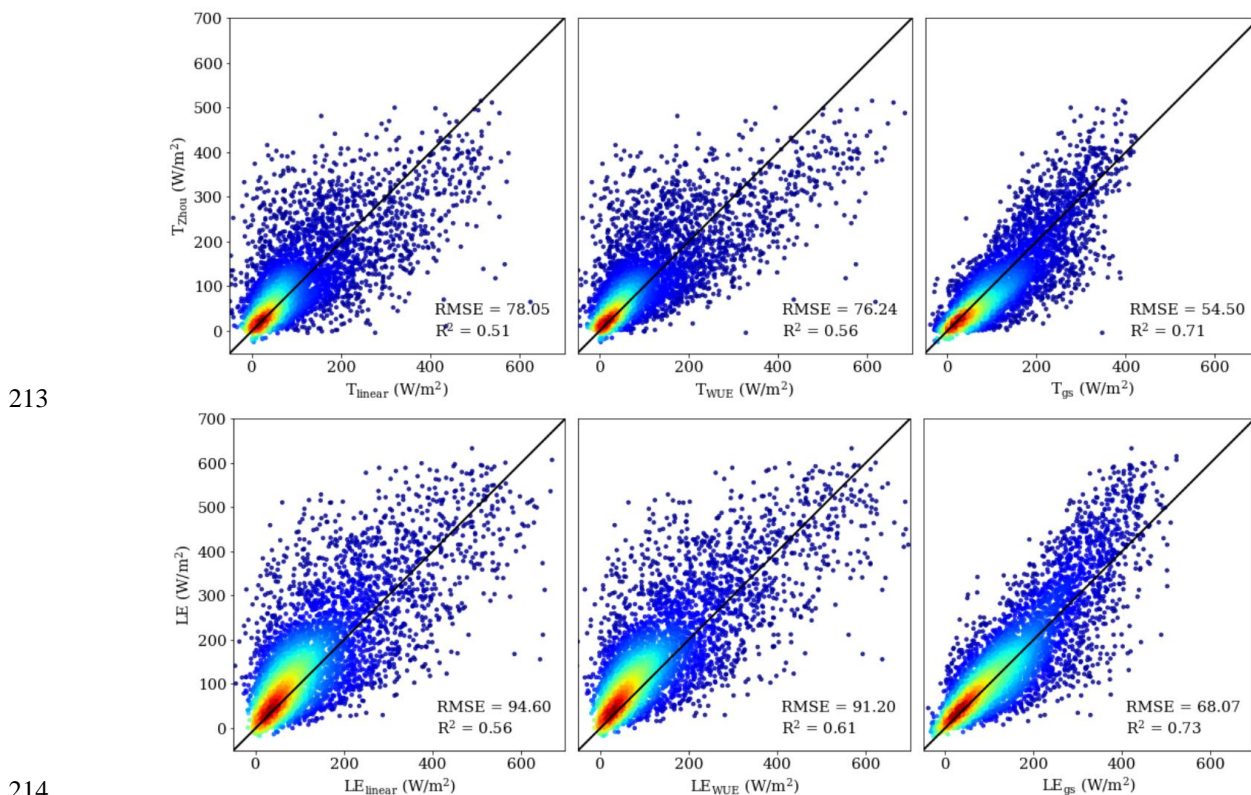
194 **3 Results**

195 **3.1 Performance of SIF- T model**

196
197 Scatter plots between reference T_{Zhou} and T modeled by SIF are shown in Figure 1 (upper
198 row). In general, both the WUE method and the conductance method improve the ability of SIF in
199 modeling T. Compared with simple linear regression with $R^2 = 0.51$ and $RMSE = 78.05 \text{ W/m}^2$, the
200 WUE model has 10% higher $R^2 = 0.56$ and 2% lower $RMSE = 76.24 \text{ W/m}^2$, while the conductance
201 model has 39% higher $R^2 = 0.71$ and 30% lower $RMSE = 54.50 \text{ W/m}^2$. The linear model and the
202 WUE model tend to overestimate T at the high values area, while most points of T_{gs} fall near the
203 1:1 line.

204 The reference T_{Zhou} may have considerable uncertainty. Plants do not always keep a specific
205 response (square root) to VPD like described in Zhou's method. Moreover, in some ecosystems,

206 the soil evaporation can not be ignored even in the peak growing season [Li *et al.*, 2019; Stoy *et*
 207 *al.*, 2019]. Here we also compared the LE derived by three SIF-T models with LE observed by
 208 eddy covariance in Fig1 (lower row). The linear model, WUE model and conductance model have
 209 $R^2 = 0.56, 0.61$ and 0.73 and $RMSE = 94.60, 91.20$ and 68.07 W/m^2 respectively. Same as
 210 compared with T_{Zhou} , the conductance model outperforms the other two models with the highest
 211 coefficients of determination and the lowest RMSE. The WUE model also has better performance
 212 than the widely used linear model.



215 **Figure 1.** Relationship of T modeled by SIF and reference latent heat (Hourly). Colors indicate
 216 the density of points (from sparse to dense: blue to red). R^2 denotes the coefficient of determination.
 217 The unit of root-mean-square deviation (RMSE) is W/m^2 . Black line denotes 1:1 line.

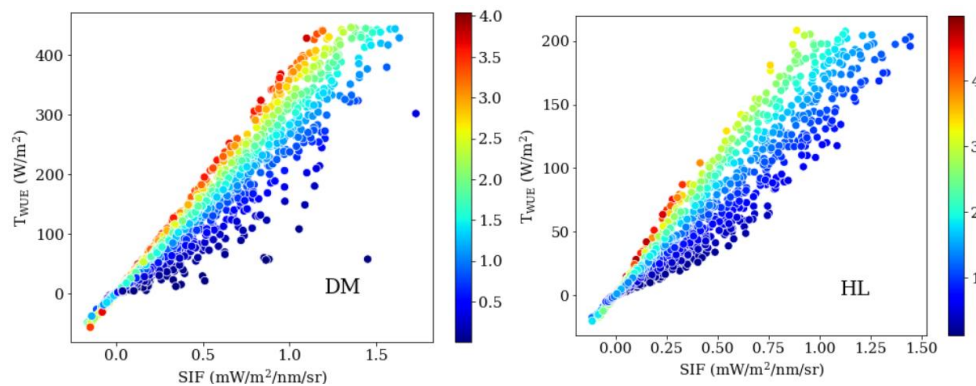
218

219 The performance of three models at different sites is shown in Table 4. When compared to
 220 T_{Zhou} , the conductance model shows the best performance at DM and HF sites with much higher
 221 $R^2 = 0.84, 0.62$, and lower $RMSE = 47.98, 77.43$ W/m^2 respectively. The linear model shows the

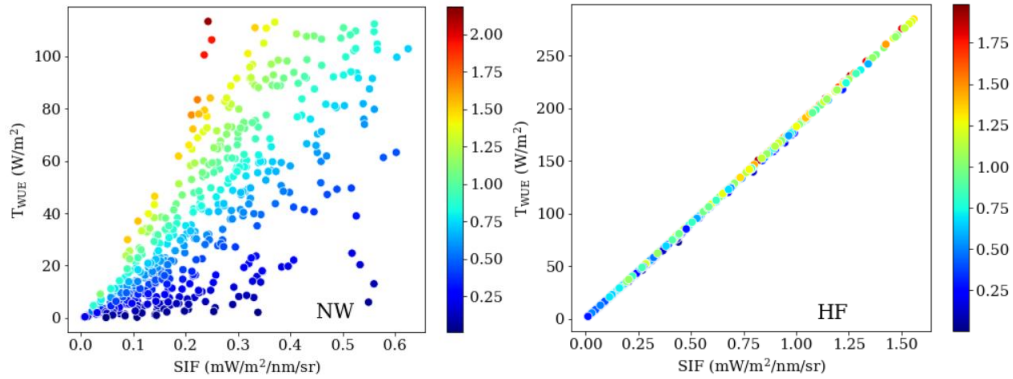
222 best performance with $R^2 = 0.58$ and $RMSE = 50.94 \text{ W/m}^2$ at the HL site. The WUE model
 223 outperforms other models at the NR site. When compared to LE observed by eddy covariance, the
 224 conductance model shows outstanding performance at all four sites. Besides, the WUE model has
 225 the lowest $RMSE = 67.38 \text{ W/m}^2$ at the NR site.

226 3.2 Sensitivity analysis of variables in two models

227 To explore what influences the relationship between SIF and T, we analyzed the sensitivity
 228 of variables in WUE and conductance models. For the WUE model, the scatterplot between SIF
 229 and T_{WUE} is shown in Figure 2. T is the product of SIF and VPD in the WUE model, which means
 230 SIF and VPD interact with each other closely and the effect of the SIF is modified by the VPD.
 231 The parameter k5 for four sites are 0.33, 0.45, 0.97, and 0.02 respectively. With the increase of
 232 VPD, the slopes of SIF-T get steeper and points get denser, while in the low VPD condition, the
 233 points are relatively sparse, which indicates the relationship between SIF and T is more linear
 234 under high VPD. Especially we find the relation between SIF and T at the HF site is not sensitive
 235 to the VPD.



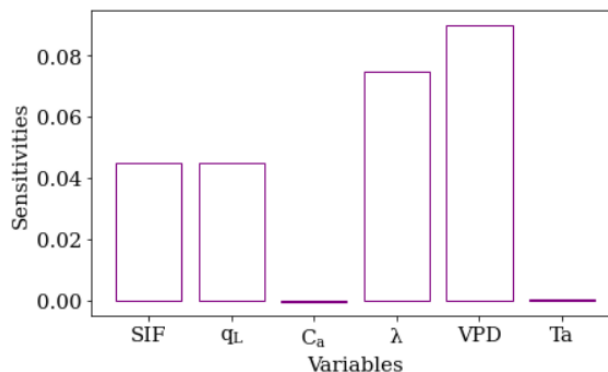
236



237

238 **Figure 2.** Scatter plot between SIF and T modeled by the WUE method. The vapor pressure deficit
 239 (VPD) has the unit kPa.

240 Atmospheric dryness is also important in modeling the stomatal behavior by SIF. For C4
 241 plants, relative humidity is used to describe the response of stomatal conductance to air dryness in
 242 the empirical Ball Berry model. For C3 plants, we investigated the sensitivities of different
 243 variables in the \mathcal{F} model by RBD-FAST-Random Balance Designs Fourier Amplitude
 244 Sensitivity Test [Tarantola *et al.*, 2006]. According to Figure 3, \mathcal{F} is sensitive to VPD, λ , SIF,
 245 and q_L . VPD exhibits the highest first-order sensitivities with values equaling 0.09, which is much
 246 higher than SIF with value 0.05. The marginal water use efficiency λ also plays an important role
 247 in \mathcal{F} with sensitivity value equaling 0.07. The fraction of open Photosynthesis II reaction centers
 248 q_L is as important as SIF (1st-order sensitivity: 0.04), which is due to the electron transport rate J
 249 is the product of SIF and q_L (Eqn 4). What's more, the gs model is not sensitive to air temperature
 250 and ambient carbon dioxide concentration. However, VPD used here is calculated by temperature
 251 and relative humidity of the air. The temperature information contained in VPD (R^2 of T_a -VPD is
 252 0.48) may impair the role of air temperature in the model. In this paper, q_L is calculated by a simple
 253 empirical equation of PAR. In fact, q_L is also related to the dark reaction but poorly studied [Baker,
 254 2008; Gu *et al.*, 2019]. More researches about q_L will improve our understanding of the
 255 relationship between SIF and J , further the SIF-GPP and SIF-T relationships.



256
257 **Figure 3.** Sensitivity analysis of variables in the stomatal conductance model \mathcal{F} of C3 plants. The
258 height of bars shows the 1st order sensitivities of different variables.

259 4 Discussion

260 Above all, the assumptions of carbon-water coupling may affect our results. Compared with
261 the linear model, though the influence of VPD on water-use efficiency is included in the WUE
262 model, soil moisture, hydraulic conductance, and other environmental variables can influence
263 water-use efficiency independently [Leakey *et al.*, 2019; Lin *et al.*, 2015; Liu *et al.*, 2020]. For the
264 conductance model, plants under stress or competition tend to change the optimal stomatal
265 conductance behavior [Wolf *et al.*, 2016]. The carbon-water economy is also influenced by traits
266 of plants and environmental variables [Bloom *et al.*, 1985; Buckley *et al.*, 2017]. This concept is
267 out of the scope of this paper, but a more physiologically based water-carbon coupling framework
268 will improve the models from the bottom up.

269 Due to the absence of direct measurements of transpiration during the research period, three
270 models were calibrated by the water budget balance framework, which might introduce uncertainty
271 to parameters, further the performance of the models. Net radiation is separated into energy
272 intercepted by canopy and soil available energy by 1D Beer's law. The simple structure of Beer's
273 law can introduce great uncertainty, especially for heterogeneity canopy and plants with leaves
274 highly anisotropic leaves in the azimuthal direction [Ponce De León and Bailey, 2019]. In the
275 conductance model, canopy available energy is also used to estimate transpiration in the two-

276 source Penman-Monteith model. So, the conductance model is more sensitive to the partition of
277 energy, in other words, suffers more uncertainty from Beer's law. Uncertainty of input data might
278 also affect our results. Firstly, VPD in the air was used to assess the aridity stress by assuming the
279 canopy and the atmosphere are fully coupled. Yet, ecosystems (DM, HL, and HF) with dense
280 closed canopy tend to decouple from the air [*De Kauwe et al.*, 2017; *Li et al.*, 2019; *Lin et al.*,
281 2018]. As both the WUE model and conductance model shows great sensitivity to VPD, using
282 VPD at the leaf scale could help to improve the performance of the SIF-T relationship. Secondly,
283 SIF data from four sites are measured by different instruments and derived by different methods
284 as mentioned above. Moreover, the FOV and heights of the observation systems vary among sites.
285 The emerge of remotely sensed SIF will fill the gap of the difference in the observation data. Last
286 but not the least, the canopy-scale SIF was directly used to model transpiration due to data
287 restriction. Nevertheless, recent papers indicated the relationship between SIF and GPP is strongly
288 affected by the structure of the canopy [*Liu et al.*, 2019; *Zeng et al.*, 2019]. We suggest
289 downscaling of SIF from the canopy scale to the photosystem scale may improve the performance
290 of the model.

291 Data from four sites were used to test the performance of the models. It is inadequate to show
292 the real potential of two models. With more and more in-situ observations from different
293 ecosystems, understanding of the underlying mechanism between SIF and T will be deepened.
294 Recently, SIF products with higher temporal-spatial resolution from different satellites, different
295 bands [*Du et al.*, 2018; *Köhler et al.*, 2018; *Köhler et al.*, 2020], and derivative products based on
296 machine learning [*Li and Xiao*, 2019; *Ma et al.*, 2020; *Yu et al.*, 2019; *Zhang et al.*, 2018] became
297 available. WUE model and conductance model can be easily combined with remote sensing ET/T
298 model like TSEB [*Norman et al.*, 1995; *Song et al.*, 2016] and PML ([*Zhang et al.*, 2019] or used

299 for assimilating SIF into a land surface model. With these data and models in this paper, estimating
 300 T via SIF at the big scale becomes promising.

301 5 Conclusion

302 In this study, in-situ hourly SIF and corresponding meteorological variables, eddy covariance
 303 observation and vegetation indexes at C3 and C4 sites were collected. Two SIF-T models based
 304 on water-use efficiency and stomatal conductance were developed and tested upon this data. Both
 305 models outperformed simple linear analysis. The WUE model has 10% higher R^2 and 2% lower
 306 RMSE, while the conductance model has the 39% higher R^2 and 30% lower RMSE. Our results
 307 indicate the SIF-T relationship depends on air dryness. These two carbon-water coupling models
 308 can be easily combined with state-of-the-art remote sensing models or land process models.
 309 Moreover, with the emergency of high temporal-spatial resolution SIF data, SIF will not only be a
 310 powerful proxy for carbon flux but also water flux at the planetary scale.

311

312

313 **Table 1.** Summary of the stations used to build models.

	Latitude	Longitude	Period	Land Cover	Reference
DM	100.37°E	38.85°N	2017.6 – 2017.9; 2018.6 – 2018.9	Maize (C4)	[Liu et al., 2018; Liu et al., 2019]
HL	115.78°E	40.33°N	2017.7 – 2017.10; 2018.7 – 2018.10	Maize (C4)	[Liu et al., 2013; Liu et al., 2019]
NR	105.55°W	40.03°N	2017.6-2017.9; 2018.6-2018.7	Mixed temperate forest (C3)	[Burns et al., 2015; Magney et al., 2019]
HF	72.17° W	42.54°N	2013.6-2013.11	Evergreen needle leaf forest(C3)	[Munger W, 2020; Yang et al., 2015]

314

315 **Table 2.** Input and intermediate variables. AWS denotes auto weather station. FAO indicates the
 316 computation methods of the variable is from <http://www.fao.org>.

Variables	Unit	Description	Source	Remarks
C_a	$\mu\text{mol/mol}$	ambient CO2 concentration	Observation	Eddy covariance
C_p	J/Kg/K	specific heat of air	1013	FAO

Non-peer reviewed EarthArXiv preprint

【This manuscript has not been submitted to any journal and not under any peer review yet】

LEs	W/m ²	Soil evaporation	$\frac{f\Delta(Rn - A_c)}{\Delta + \gamma}$	[Fisher et al., 2008]
f	-	Soil evaporation constraint	SM/(SM _{max} - SM _{min})	-
ga	m/s	Aerodynamic conductance	$\frac{1}{v/(u^*)^2 + 6.2(u^*)^{-2/3}}$	[Monteith and Unsworth, 2013]
GPP_{ob}	μmol/m ² /s	Gross primary production	Separated from NEE observed by eddy covariance	[Lasslop et al., 2010; Reichstein et al., 2005]
LE	W/m ²	Latent heat	Observation	Eddy covariance
PAR	W/m ²	photosynthetically active radiation	Observation	AWS
P	kPa	Air Pressure	Observation	AWS
q_L	-	Fraction of open Photosynthesis II reaction centers	exp(-β PAR)	This paper
Rh	-	Relative humidity	Observation	AWS
Rn	W/m ²	Net radiation	Observation	AWS
SIF	mW/m ² /sr/nm	Sun-induced chlorophyll fluorescence	Observation	-
SM	%	Soil moisture	Observation	Thermal Dissipation Probe
Ta	°C	Air temperature	Observation	AWS
u*	m/s	Friction Velocity	Observation	Eddy covariance
v	m/s	Wind speed	Observation	AWS
VPD	kPa	Vapor pressure deficit	$(100 - Rh)/100 \times 0.6108 \times \exp(17.27 Ta/(Ta + 237.3))$	FAO
Δ	kPa/K	Slope of saturation vapor pressure curve	$(2503 \exp(17.27 Ta/(Ta + 237.3))) / ((Ta + 237.3)^2)$	FAO
γ	kPa/K	psychrometric constant	0.665 × 0.001P	FAO
Γ	μmol/mol	CO2 compensation point in the absence of mitochondrial	36.9 + 1.18(Ta - 25) + 0.036(Ta - 25) ² for C3; 0 for C4	[Katul et al., 2010]
ρ_a	kg/m ³	Air density	1.292 - 0.00428 Ta	FAO

318 **Table 3.** Parameters needed to be calibrated.
319

	Parameter	Lower	Upper	Reference
Linear model	K1	5	50	[Liu et al., 2017; Sun et al., 2017]
	K2	3	50	[Huang et al., 2016]
WUE model	K3	5	50	[Liu et al., 2017; Sun et al., 2017]
	K4	3	30	[Zhou et al., 2015]; This paper
	K5	0	1	[Lin et al., 2018]
Conductance model (C4)	β	0	0.001	This paper; [Gu et al., 2019]
	a	10	300	This paper
	m	2.5	8.8	[Miner et al., 2017]
Conductance model (C3)	β	0	0.01	This paper; [Gu et al., 2019; Katul et al., 2010]
	a	10	300	This paper
	λ	10	200	[Cowan and GD, 1977; Katul et al., 2010]

320

321 **Table 4.** Coefficient of determination (R^2) and root mean square error (RMSE) at different sites.
322 Best values are marked with the bold font.

	Reference	DM		HL		NR		HF	
		R^2	RMSE	R^2	RMSE	R^2	RMSE	R^2	RMSE
T_{linear}		0.46	104.25	0.58	50.94	0.49	35.32	0.45	70.66
T_{WUE}	T_{Zhou}	0.55	99.11	0.55	53.66	0.69	29.26	0.45	71.80
T_{gs}		0.84	47.98	0.57	54.79	0.46	41.27	0.62	77.43
LE_{linear}		0.56	119.97	0.52	67.69	0.27	68.69	0.44	81.92
LE_{WUE}	LE	0.55	114.20	0.55	66.71	0.36	67.38	0.44	84.87
LE_{gs}		0.87	69.36	0.60	64.53	0.40	68.82	0.55	70.71

323

324

References:

- 325 Alemohammad, S. H., et al. (2017), Water, Energy, and Carbon with Artificial Neural Networks (WECANN): a
326 statistically based estimate of global surface turbulent fluxes and gross primary productivity using solar-induced
327 fluorescence, *BIOGEOSCIENCES*, 14(18), 4101-4124.
- 328 Bai, Y., et al. (2019), Quantifying plant transpiration and canopy conductance using eddy flux data: An underlying
329 water use efficiency method, *AGR FOREST METEOROL*, 271, 375-384.
- 330 Baker, N. R. (2008), Chlorophyll Fluorescence: A Probe of Photosynthesis In Vivo, *ANNU REV PLANT BIOL*, 59(1),
331 89-113.
- 332 Ball, J. T., et al. (1987), A model predicting stomatal conductance and its contribution to the control of photosynthesis
333 under different environmental conditions, in *Progress in photosynthesis research*, edited, pp. 221-224, Springer.
- 334 Beer, C., et al. (2009), Temporal and among-site variability of inherent water use efficiency at the ecosystem level,
335 *GLOBAL BIOGEOCHEM CY*, 23(2), n/a-n/a.
- 336 Berry, J. A., et al. (2010), Stomata: key players in the earth system, past and present, *CURR OPIN PLANT BIOL*,
337 13(3), 232-239.
- 338 Bloom, A. J., et al. (1985), Resource limitation in plants-an economic analogy, *Annual review of Ecology and*

- 339 *Systematics*, 16(1), 363-392.
- 340 Buckley, T. N., et al. (2017), Optimal plant water economy, *Plant, Cell & Environment*, 40(6), 881-896.
- 341 Burns, S. P., et al. (2015), The influence of warm-season precipitation on the diel cycle of the surface energy balance
342 and carbon dioxide at a Colorado subalpine forest site, *BIOGEOSCIENCES*, 12(23), 7349-7377.
- 343 Collatz, G. J., et al. (1992), Coupled photosynthesis-stomatal conductance model for leaves of C4 plants, *FUNCT*
344 *PLANT BIOL*, 19(5), 519-538.
- 345 Cowan, I. R., and F. GD (1977), Stomatal function in relation to leaf metabolism and environment.
- 346 Damm, A., et al. (2015), Far-red sun-induced chlorophyll fluorescence shows ecosystem-specific relationships to
347 gross primary production: An assessment based on observational and modeling approaches, *REMOTE SENS*
348 *ENVIRON*, 166, 91-105.
- 349 De Kauwe, M. G., et al. (2017), Ideas and perspectives: how coupled is the vegetation to the boundary layer?
350 *BIOGEOSCIENCES*, 14(19), 4435-4453.
- 351 Du, S., et al. (2018), Retrieval of global terrestrial solar-induced chlorophyll fluorescence from TanSat satellite, *SCI*
352 *BULL*, 63(22), 1502-1512.
- 353 Duan, Q., et al. (1994), Optimal use of the SCE-UA global optimization method for calibrating watershed models, *J*
354 *HYDROL*, 158(3-4), 265-284.
- 355 Fisher, J. B., et al. (2008), Global estimates of the land - atmosphere water flux based on monthly AVHRR and
356 ISLSCP-II data, validated at 16 FLUXNET sites, *REMOTE SENS ENVIRON*, 112(3), 901-919.
- 357 Frankenberg, C., and J. Berry (2018), Solar induced chlorophyll fluorescence: Origins, relation to photosynthesis and
358 retrieval.
- 359 Gentine, P., et al. (2019), Coupling between the terrestrial carbon and water cycles—a review, *ENVIRON RES LETT*,
360 14(8), 83003.
- 361 Good, S. P., et al. (2015), WATER RESOURCES. Hydrologic connectivity constrains partitioning of global terrestrial
362 water fluxes, *SCIENCE*, 349(6244), 175-177.
- 363 Gorelick, N., et al. (2017), Google Earth Engine: Planetary-scale geospatial analysis for everyone, *REMOTE SENS*
364 *ENVIRON*, 202, 18-27.
- 365 Gu, L., et al. (2019), Sun-induced Chl fluorescence and its importance for biophysical modeling of photosynthesis
366 based on light reactions, *NEW PHYTOL*, 223(3), 1179-1191.
- 367 Guanter, L., et al. (2014), Global and time-resolved monitoring of crop photosynthesis with chlorophyll fluorescence,
368 *Proceedings of the National Academy of Sciences*, 111(14), E1327-E1333.
- 369 Harris, C. R., et al. (2020), Array programming with NumPy, *NATURE*, 585(7825), 357-362.
- 370 Herman, J., and W. Usher (2017), SALib: an open-source Python library for sensitivity analysis, *Journal of Open*
371 *Source Software*, 2(9), 97.
- 372 Houska, T., et al. (2015), SPOTting model parameters using a ready-made python package, *PLOS ONE*, 10(12),
373 e145180.
- 374 Huang, M., et al. (2016), Seasonal responses of terrestrial ecosystem water-use efficiency to climate change, *GLOBAL*
375 *CHANGE BIOL*, 22(6), 2165-2177.
- 376 Jasechko, S., et al. (2013), Terrestrial water fluxes dominated by transpiration, *NATURE*, 496(7445), 347-350.
- 377 Jonard, F., et al. (2020), Value of sun-induced chlorophyll fluorescence for quantifying hydrological states and fluxes:
378 Current status and challenges, *AGR FOREST METEOROL*, 291, 108088.
- 379 Katul, G., et al. (2010), A stomatal optimization theory to describe the effects of atmospheric CO2 on leaf
380 photosynthesis and transpiration, *ANN BOT-LONDON*, 105(3), 431-442.
- 381 Köhler, P., et al. (2018), Global Retrievals of Solar - Induced Chlorophyll Fluorescence With TROPOMI: First
382 Results and Intersensor Comparison to OCO - 2, *GEOPHYS RES LETT*, 45(19), 10, 410-456, 463.
- 383 Köhler, P., et al. (2020), Global Retrievals of Solar - Induced Chlorophyll Fluorescence at Red Wavelengths With
384 TROPOMI, *GEOPHYS RES LETT*, 47(15).
- 385 Kool, D., et al. (2014), A review of approaches for evapotranspiration partitioning, *AGR FOREST METEOROL*, 184,
386 56-70.
- 387 Lasslop, G., et al. (2010), Separation of net ecosystem exchange into assimilation and respiration using a light response
388 curve approach: critical issues and global evaluation, *GLOBAL CHANGE BIOL*, 16(1), 187-208.
- 389 Leakey, A., et al. (2019), Water Use Efficiency as a Constraint and Target for Improving the Resilience and
390 Productivity of C3 and C4 Crops, *ANNU REV PLANT BIOL*, 70, 781-808.
- 391 Leuning, R., et al. (2008), A simple surface conductance model to estimate regional evaporation using MODIS leaf
392 area index and the Penman-Monteith equation, *WATER RESOUR RES*, 44(10).
- 393 Li, X., et al. (2018), Solar-induced chlorophyll fluorescence is strongly correlated with terrestrial photosynthesis for

- 394 a wide variety of biomes: First global analysis based on OCO-2 and flux tower observations, *GLOBAL CHANGE*
 395 *BIOL*, 24(9), 3990-4008.
- 396 Li, X., et al. (2019), A simple and objective method to partition evapotranspiration into transpiration and evaporation
 397 at eddy-covariance sites, *AGR FOREST METEOROL*, 265, 171-182.
- 398 Li, X., and J. Xiao (2019), A Global, 0.05-Degree Product of Solar-Induced Chlorophyll Fluorescence Derived from
 399 OCO-2, MODIS, and Reanalysis Data, *REMOTE SENS-BASEL*, 11(5), 517.
- 400 Lin, C., et al. (2018), Diel ecosystem conductance response to vapor pressure deficit is suboptimal and independent
 401 of soil moisture, *AGR FOREST METEOROL*, 250-251, 24-34.
- 402 Lin, Y., et al. (2015), Optimal stomatal behaviour around the world, *NAT CLIM CHANGE*, 5(5), 459-464.
- 403 Liu, L., et al. (2017), Directly estimating diurnal changes in GPP for C3 and C4 crops using far-red sun-induced
 404 chlorophyll fluorescence, *AGR FOREST METEOROL*, 232, 1-9.
- 405 Liu, S., et al. (2018), The Heihe Integrated Observatory Network: A Basin-Scale Land Surface Processes Observatory
 406 in China, *VADOSE ZONE J*, 17(1), 180021-180072.
- 407 Liu, S. M., et al. (2013), Measurements of evapotranspiration from eddy-covariance systems and large aperture
 408 scintillometers in the Hai River Basin, China, *J HYDROL*, 487, 24-38.
- 409 Liu, X., et al. (2019), Downscaling of solar-induced chlorophyll fluorescence from canopy level to photosystem level
 410 using a random forest model, *REMOTE SENS ENVIRON*, 231, 110772.
- 411 Liu, X., et al. (2019), Atmospheric Correction for Tower-Based Solar-Induced Chlorophyll Fluorescence Observations
 412 at O2-A Band, *REMOTE SENS-BASEL*, 11(3), 355.
- 413 Liu, X., et al. (2020), Improving the potential of red SIF for estimating GPP by downscaling from the canopy level to
 414 the photosystem level, *AGR FOREST METEOROL*, 281, 107846.
- 415 Liu, Y., et al. (2020), Plant hydraulics accentuates the effect of atmospheric moisture stress on transpiration, *NAT*
 416 *CLIM CHANGE*, 10(7), 691-695.
- 417 Lu, X., et al. (2018), Potential of solar-induced chlorophyll fluorescence to estimate transpiration in a temperate forest,
 418 *AGR FOREST METEOROL*, 252, 75-87.
- 419 Ma, Y., et al. (2020), Generation of a Global Spatially Continuous TanSat Solar-Induced Chlorophyll Fluorescence
 420 Product by Considering the Impact of the Solar Radiation Intensity, *REMOTE SENS-BASEL*, 12(13), 2167.
- 421 Maes, W. H., et al. (2020), Sun-induced fluorescence closely linked to ecosystem transpiration as evidenced by
 422 satellite data and radiative transfer models, *REMOTE SENS ENVIRON*, 249, 112030.
- 423 Magney, T. S., et al. (2019), Mechanistic evidence for tracking the seasonality of photosynthesis with solar-induced
 424 fluorescence, *Proceedings of the National Academy of Sciences*, 201900278.
- 425 Miner, G. L., et al. (2017), Estimating the sensitivity of stomatal conductance to photosynthesis: a review, *Plant, Cell*
 426 *& Environment*, 40(7), 1214-1238.
- 427 Monteith, J., and M. Unsworth (2013), Principles of environmental physics: plants, animals, and the atmosphere.
- 428 Munger W, W. S. (2020), Canopy-Atmosphere Exchange of Carbon, Water and Energy at Harvard Forest EMS Tower
 429 since 1991. Harvard Forest Data Archive: HF004., edited.
- 430 Myneni, R., et al. (2015), MCD15A3H MODIS/Terra+ Aqua Leaf Area Index/FPAR 4-day L4 Global 500m SIN Grid
 431 V006., edited.
- 432 Norman, J. M., et al. (1995), Source approach for estimating soil and vegetation energy fluxes in observations of
 433 directional radiometric surface temperature, *AGR FOREST METEOROL*, 77(3-4), 263-293.
- 434 Pagán, B., et al. (2019), Exploring the Potential of Satellite Solar-Induced Fluorescence to Constrain Global
 435 Transpiration Estimates, *REMOTE SENS-BASEL*, 11(4), 413.
- 436 Ponce De León, M. A., and B. N. Bailey (2019), Evaluating the use of Beer's law for estimating light interception in
 437 canopy architectures with varying heterogeneity and anisotropy, *ECOL MODEL*, 406, 133-143.
- 438 Reichstein, M., et al. (2005), On the separation of net ecosystem exchange into assimilation and ecosystem respiration:
 439 review and improved algorithm, *GLOBAL CHANGE BIOL*, 11(9), 1424-1439.
- 440 Ryu, Y., et al. (2019), What is global photosynthesis? History, uncertainties and opportunities, *REMOTE SENS*
 441 *ENVIRON*, 223, 95-114.
- 442 Schimel, D., et al. (2019), Flux towers in the sky: global ecology from space, *NEW PHYTOL*, 224(2), 570-584.
- 443 Scott, R. L., and J. A. Biederman (2017), Partitioning evapotranspiration using long-term carbon dioxide and water
 444 vapor fluxes, *GEOPHYS RES LETT*, 44(13), 6833-6840.
- 445 Shan, N., et al. (2019), Modeling canopy conductance and transpiration from solar-induced chlorophyll fluorescence,
 446 *AGR FOREST METEOROL*, 268, 189-201.
- 447 Song, L., et al. (2016), Applications of a thermal-based two-source energy balance model using Priestley-Taylor
 448 approach for surface temperature partitioning under advective conditions, *J HYDROL*, 540, 574-587.
- 449 Stoy, P. C., et al. (2019), Reviews and syntheses: Turning the challenges of partitioning ecosystem evaporation and

450 transpiration into opportunities, *BIOGEOSCIENCES*, 16(19), 3747-3775.
451 Sun, Y., et al. (2017), OCO-2 advances photosynthesis observation from space via solar-induced chlorophyll
452 fluorescence, *SCIENCE*, 358(6360), m5747.
453 Tarantola, S., et al. (2006), Random balance designs for the estimation of first order global sensitivity indices, *RELIAB*
454 *ENG SYST SAFE*, 91(6), 717-727.
455 Tol, C., et al. (2014), Models of fluorescence and photosynthesis for interpreting measurements of solar - induced
456 chlorophyll fluorescence, *Journal of Geophysical Research: Biogeosciences*, 119(12), 2312-2327.
457 Way, D. A., et al. (2014), Increasing water use efficiency along the C3 to C4 evolutionary pathway: a stomatal
458 optimization perspective, *J EXP BOT*, 65(13), 3683-3693.
459 Wolf, A., et al. (2016), Optimal stomatal behavior with competition for water and risk of hydraulic impairment,
460 *Proceedings of the National Academy of Sciences*, 113(46), E7222-E7230.
461 Wolz, K. J., et al. (2017), Diversity in stomatal function is integral to modelling plant carbon and water fluxes, *NAT*
462 *ECOL EVOL*, 1(9), 1292-1298.
463 Yang, X., et al. (2015), Solar-induced chlorophyll fluorescence that correlates with canopy photosynthesis on diurnal
464 and seasonal scales in a temperate deciduous forest, *GEOPHYS RES LETT*, 42(8), 2977-2987.
465 Yang, Y., et al. (2015), An analytical model for relating global terrestrial carbon assimilation with climate and surface
466 conditions using a rate limitation framework, *GEOPHYS RES LETT*, 42(22), 9825-9835.
467 Yu, L., et al. (2019), High - Resolution Global Contiguous SIF of OCO - 2, *GEOPHYS RES LETT*, 46(3), 1449-1458.
468 Yuan, W., et al. (2007), Deriving a light use efficiency model from eddy covariance flux data for predicting daily
469 gross primary production across biomes, *AGR FOREST METEOROL*, 143(3-4), 189-207.
470 Zeng, Y., et al. (2019), A practical approach for estimating the escape ratio of near-infrared solar-induced chlorophyll
471 fluorescence, *REMOTE SENS ENVIRON*, 232, 111209.
472 Zhang, Y., et al. (2014), Estimation of vegetation photosynthetic capacity from space-based measurements of
473 chlorophyll fluorescence for terrestrial biosphere models, *GLOBAL CHANGE BIOL*, 20(12), 3727-3742.
474 Zhang, Y., et al. (2018), A global spatially contiguous solar-induced fluorescence (CSIF) dataset using neural
475 networks, *BIOGEOSCIENCES*, 15(19), 5779-5800.
476 Zhang, Y., et al. (2019), Coupled estimation of 500 m and 8-day resolution global evapotranspiration and gross
477 primary production in 2002 - 2017, *REMOTE SENS ENVIRON*, 222, 165-182.
478 Zhang, Z., et al. (2020), Reduction of structural impacts and distinction of photosynthetic pathways in a global
479 estimation of GPP from space-borne solar-induced chlorophyll fluorescence, *REMOTE SENS ENVIRON*, 240, 111722.
480 Zhou, S., et al. (2014), The effect of vapor pressure deficit on water use efficiency at the subdaily time scale,
481 *GEOPHYS RES LETT*, 41(14), 5005-5013.
482 Zhou, S., et al. (2015), Daily underlying water use efficiency for AmeriFlux sites, *Journal of Geophysical Research:*
483 *Biogeosciences*, 120(5), 887-902.
484 Zhou, S., et al. (2018), Water use efficiency and evapotranspiration partitioning for three typical ecosystems in the
485 Heihe River Basin, northwestern China, *AGR FOREST METEOROL*, 253-254, 261-273.
486